Transactions, **SMiRT-25**
Charlotte, NC, USA, August 4-9, 2019
Division III (Computation, Simulation, and Visualization)

COMPARISON OF CALCULATED AND MEASURED STRAINS IN THE MICROSTRUCTURE OF STEEL 316L

M. Niffenegger[1], V. Herrera-Solaz[2]

[1] Senior Scientist, Laboratory for Materials Behavior, Nuclear Energy and Safety Research Department, Paul Scherrer Institute, 5232 Villigen PSI, Switzerland (Markus.Niffenegger@psi.ch)
[2] Postdoctoral Fellow, Laboratory for Materials Behavior, Nuclear Energy and Safety Research Department, Paul Scherrer Institute, 5232 Villigen PSI, Switzerland

ABSTRACT

The SNF model for the calculation of crack networks and to estimate crack initiation site and crack propagation through the anisotropic microstructure of austenitic stainless steel AISI 316L was developed at Paul Scherrer Institut (PSI) in Switzerland (PSI). This hysteresis energy-based mesoscale model uses the sizes and crystallographic orientations of the grains, measured with electron back scattering diffraction (EBSD). The anisotropic elastic properties of a representative volume element (RVE) and the anisotropic plastic behavior of each single crystal, defined through the evolution of shear deformation in the slip plane with the highest Schmid factor, is considered. Concerning properties are preliminary determined by a standard tensile test. A four-parameter damage model used for crack initiation and growth, based on the accumulated inelastic hysteresis energy, was implemented. This model allows the calculation of stresses and strains in the microstructure, the calculation of high and low cycle fatigue lifetime, and performing sensitivity studies such as the influence of e.g. grain sizes on stress-strain curves.

In this paper, we compare local strains and stresses in the microstructure, calculated by the SNF model and by the crystal plasticity finite element (CPFEM) code CAPSUL with those measured with a Digital Image Correlation System (DIC). Good agreement of calculated strains with measured ones were observed for strain up to about 4% for SNF and CPFEM method, whereas the latter is more accurate for larger strains.

INTRODUCTION

Thermo-mechanical fatigue (TMF) is a well-known phenomenon. In nuclear power plants (NPPs) TMF appears in the low cycle (LCF) or/and high cycle fatigue (HCF) regime, often connected with operating transients. Whereas LCF damage is covered by existing safety assessment rules and codes, stratification due to temperature differences in horizontal tubes are partially covered by national rules. However, turbulent mixing of cold and hot water flow, causing cyclic thermal shocks (CTS) on the inner piping wall of e.g. mixing tees (LCF and HCF), is not covered by design rules and therefore not anticipated at the design stage. Damage due to CTS in T-junctions has been reported, Metzner (2005), NEA/CSNI/R (2005) and OECD (2006). Such CTS caused by the unstable turbulent flow, is leading to temperature fluctuations at the inner wall of the piping where they induce thermal stresses, which may end up in a network of micro cracks (called elephant skin or crazing). This crazing is characteristic for the biaxial stress/strain loading as it appears due to thermal shock loads, often superimposed to other loads, e.g. internal pressure or residual stresses in welded tubes. Although most micro cracks arrest in a depth of a few millimeter, under certain circumstances, some of them may grow through the wall as reported in several publications e.g. Faidy (2000), Cipiere et al. (2001), Hirschberg (2000) and Deardorff (2004).

At the Paul Scherrer Institute (PSI), we address this topic within the research project PLiM, which is dedicated to the experimental and theoretical investigation of TMF due to CTS and to the thermo-hydraulic prediction of turbulent fluid flow leading to these CTS, Janssens et al. (2008) and Niffenegger et al. (2009). The overall aim of these investigations is to acquire a better understanding of the governing mechanisms and to improve numerical tools for the prediction of component's lifetime.

Cyclic thermo-shock experiments on flat, un-notched and biaxial-mechanically loaded specimens, performed at PSI, reproduce the formation of crack networks observed in NPPs under well-defined laboratory conditions, Niffenegger, Herrera-Solaz (2017).

In this paper we focus on the calculation of local stress/strains by means of the micro-structural based finite element (FE) model for fatigue (SNF), developed by Sistaninia & Niffenegger (2014, 2015) and further extended by Herrera & Niffenegger (2017). The SNF model allows investigating the influence of grain size, grain orientation and geometry, boundary constrains and initial defects on the crack initiation site, the development of crack networks and fatigue lifetime of steels, by considering the material's microstructure measured by Electron Back Scatter Diffraction (EBS). In particular, we report on the validation of calculated stress/strains on the grain size level with the SNF model by comparing computational results with those from the more sophisticated crystal plasticity finite element model (CPFEM) CAPSUL, Segurado and LLorca (2013), and those from Digital Image Correlation (DIC) measurements.

The structure of this article as follows. First, we describe the basis of the SNF and CPFEM models. Secondly, we present the sample preparation, experimental procedure and finally we discuss the experimental and numerical results and conclusions.

THE MICROSTRUCTURAL BASED NUMERICAL FATIGUE MODEL SNF

The SNF fatigue model considers the real microstructure of the material. This mesoscale model uses the sizes and crystallographic orientations of the grains, measured with electron back scattering diffraction (EBSD). The anisotropic elastic properties of a representative volume element (RVE) and the anisotropic plastic behavior of each single crystal, defined through the evolution of shear deformation in the slip plane with the highest Schmid factor, is considered. Concerning material properties are preliminary determined by a standard tensile test. A four parameter damage model (DM) used for crack initiation and growth, based on the accumulated inelastic hysteresis energy, has been implemented.

The SNF model allows the calculation of inhomogeneous stresses and strains in the microstructure, the calculation of LCF and HCF lifetime, and performing sensitivity studies such as the influence of e.g. grain sizes on stress-strain curves. Crack initiation and growth is controlled by the inelastic hysteresis energy, following the Darveaux (2002) model, whereas the slip system is evaluated based on the dominant resolved shear stress. The procedure following the SNF is:

1. Measuring the microstructure by EBSD to determine the grain geometry and orientation.
2. Transfer of the actual crystallographic orientation obtained with EBSD into the input file of the FE code Abaqus.
3. Generation of the FE-model (Representative Volume Element, RVE), in which each grain has its specific anisotropic material properties and crystallographic orientation. A routine automatically creates a thin 3D polyhedral model of the microstructure for analyzing by the FE solver. This routine reads the 2D EBSD data, i.e. the position and orientation (Euler angles) for each points of the selected specimen's surface. A randomly oriented (not columnar) extrusion of the planar geometry in thickness direction of the sample defines the FE nodes, elements and material. The advantages of this kind of 3D model (randomly extruded) are that the created grains are more realistic than planar or columnar ones and built faster than a full 3D-model, which needs very time-consuming 3D EBSD measurements and special modeling tools.

   The resolution of the EBSD maps is typically in the micrometer range. Every EBSD point is assigned to one eight-node brick element, resulting in a fine FE-mesh. No special elements at the grain boundaries are used to account for the deformation process, meaning that common element nodes of neighboring grains tightly couples the grains. This is a reasonable approximation in the low temperature range, where grain boundary sliding is negligible.

4. Transformation of material properties from crystal to the global coordinate system. The orthogonal-anisotropic elastic tensor of the face centered cubic (FCC) crystals can be specified in terms of three elastic moduli C_{11} (C_{1111}=C_{2222}=C_{3333}), C_{12} (C_{1122}=C_{1133}=C_{2233}) and C_{44} (C_{1212}=C_{1313}=C_{2323}), given in Tab. 1. Since the crystal coordinate systems $x_iy_iz_i$ (i=1,2,…n; where n is the number of grains in the RVE), differs from the global coordinate system of the FE-model XYZ, the elastic constants C_{mnpq} are transformed from the individual crystal coordinate systems $x_iy_iz_i$ to the global (FE) coordinate system XYZ by

$$C'_{ijkl} = a_{im}a_{jn}a_{kp}a_{lq}C_{mnpq} \tag{1}$$

In Eq. 1 the Einstein's summation convention over the indices (i, j, k, l, m, n, p, q, taking the values 1, 2, 3,) is used, where the a_{ij} are the concerning components of the rotation matrix.

5. Calculation of the fatigue behavior as a function of the number of cycles by employing the inelastic hysteresis energy criterion and the "direct cyclic approach" implemented in Abaqus (2014). In ductile materials under cyclic stress-strain load, accumulated plastic shear deformation is responsible for fatigue degradation. This degradation is accomplished by means of a scalar damage variable D, which acts via the stress tensor σ, defining the stress of the damaged material σ_d for each integration point of the FE-mesh as

$$\sigma_d = (1-D)\sigma \tag{2}$$

Calculation of the initiation of damage in a FE and the evolution of D by means of the inelastic hysteresis energy ΔW within one cycle. Note that D=0 corresponds to no damage and D=1 to fully damaged material, respectively. The number of cycles N_i up to the onset of damage is

$$N_i = A\Delta W^B \tag{3}$$

and the evolution of D is

$$\frac{dD}{dN} = \frac{k_1 \Delta W^{k_2}}{L} \tag{4}$$

The parameters A, B, k_1 and k_2, of the damage model (summarized in Tab.1) are material specific and determined from fatigue tests by means of the Levenberg-Marquardt algorithm, Herrera-Solaz and Niffenegger (2017). The characteristic length L, typically measures the diagonal between two integration points of the FE, which makes the change of the hysteresis energy independent from mesh size.

In case of monotonic loading conditions, the plastic behavior of a polycrystal is approximated by the Taylor relationship (1938) between the tensile yield strength σ_y and the initial critical resolved shear stress $\tau_{0,c}$ for a single crystal following

$$\sigma_y = \tau_{0,c} \cdot \sum_{i=1}^{N} \frac{v_i}{m^i} = \tau_{0,c} \cdot \frac{1}{\overline{m}} = \tau_{0,c} \cdot \overline{M} \tag{5}$$

where v_i represents the volume-weight for each crystal i and $\overline{m}$ the average Schmid factor for the polycrystal. Following relation (6), a von Mises criterion is employed to define the yielding of each single crystal by means of a yield strength σ_y^i and the initial critical resolved shear stress $\tau_{0,c}$, as

$$\sigma_y^i = \frac{\tau_{0,c}}{m^i} = \sqrt{3J_2} \tag{6}$$

in a way that the yield strength of the polycrystal σ_y remains as

$$\sigma_y = \sum_{i=1}^{N} v_i \cdot \sigma_y^i = \tau_{0,c} \cdot \sum_{i=1}^{N} \frac{v_i}{m^i} \tag{7}$$

Furthermore, an isotropic hardening law is defined for each single crystal i by means of $h_0^i, \sigma_y^i, \sigma_{sat}^i$ and the hardening exponent a, as

$$\frac{d\sigma^i}{d\epsilon^i}(\sigma^i \geq \sigma_y^i) = h_0^i\left(1 - \frac{\sigma^i - \sigma_y^i}{\sigma_{sat}^i - \sigma_y^i}\right)^a \tag{8}$$

where h_0^i, σ_{sat}^i and ϵ^i are

$$\sigma_{sat}^i = \frac{\tau_{sat}}{m^i}; h_0^i = \frac{h_0}{m^i}; \epsilon^i = \gamma \cdot m^i \tag{9}$$

THE CRYSTAL PLASTICITY MODEL

The CPFEM model is implemented as a user subroutine CAPSUL in the finite element code Abaqus, Segurado, LLorca (2013), Herrera-Solaz et al. (2014). The anisotropic elastic deformation of the grains is considered as in the SNF code, but plastic deformation along all slip systems α is taken into account. Note that in the SNF model only the slip system with the highest Schmidt factor is active.

In the CPFEM model, the deformation gradient is decomposed into an elastic and plastic part, $\mathbf{F}^e$ and $\mathbf{F}^p$. The adopted behavior of the crystals follows an elasto-viscoplastic model, in which the shear rate for a given slip system α, $\dot{\gamma}^\alpha$, is obtained by a power-law according to, Kothari and Anand (1998)

$$\dot{\gamma}^\alpha = \dot{\gamma}_0\left(\frac{|\tau^\alpha|}{\tau_c^\alpha}\right)^{\frac{1}{m}} sign(\tau^\alpha) \tag{10}$$

where $\dot{\gamma}_0$ is the reference shear strain rate, τ^α the resolved shear stress of the slip system α, m the rate-sensitivity exponent and τ_c^α the critical resolved shear stress on the slip system α. τ^α is calculated by projecting the Piola-Kirchhoff stress tensor $\boldsymbol{S}$ on the slip system α according to

$$\tau^\alpha = S: s^\alpha \otimes m^\alpha \tag{11}$$

A phenomenological hardening model to mimic the different stages of single crystal deformation, Taylor (1938), has been implemented. The initial value of the critical resolved shear stress τ_c^α of slip system α is given by $\tau_{0,c}$ and its evolution due to slip follows as

$$\dot{\tau}_c^\alpha = q\sum_{j=1}^{N} h_{0,j}\left(1 - \frac{\tau^j}{\tau_{sat}^j}\right)^a |\dot{\gamma}^j| \tag{12}$$

where the different parameters in this equation define the contribution from self- and latent-hardening. The self-hardening is defined by three terms, the saturation stress τ_{sat}, the initial hardening rate h_0 and the hardening exponent a. The latent-hardening is considered with the coefficient q. For the austenitic stainless steel 316L we used the parameters given in Tab. 1.

Tab. 1: Parameters used for AISI 316L

Parameter	C_{11} [GPa]	C_{12} [GPa]	C_{44} [GPa]	$\tau_{0,c}$ [MPa]	τ_{sat} [MPa]	h_0 [MPa]	**A** [-]	**B** [-]	**k_1** [-]	k_2 [-]	$\dot{\gamma}_0$ [s^{-1}]	m [-]	a [-]	q [-]
CP	197.5	125	122	65	280	360					1.0	0.02	1.0	1.0
SNF	197.5	125	122	48	654	117	$6.42\cdot10^3$	$6.52\cdot10^3$	$6\cdot10^{-2}$	$1.51\cdot10^3$	1.0	0.02	1.0	1.0

EXPERIMENTAL PROCEDURE

Special flat hourglass shaped tensile specimen with a cross section of 4 mm width, 4.7 mm thickness and a total specimen's length of 160 mm, shown in Fig. 1, was prepared in order to perform in-situ and ex-situ strain measurements with a digital image correlation (DIC) system. The specimen are made of AISI 316L, an austenitic stainless steel with a chemical composition (in wt%) of 0.018 C, 0.42 Si, 1.68 Mn, 0.015 P, 0.001S and 17.6 Cr. This steel is widely used in nuclear industry due to its good mechanical and chemical properties such as ductility and resistance against corrosion. In order to increase the experimental resolution, from the original (as-received) material with an average grain size of 17 µm, an average grain size of 1625 μm has been prepared by a heat treatment. This was achieved by heating the specimen under a controlled heating rate of 200°C/h up to a temperature of 1300°C, holding this temperature for 24h, before cooling down with a rate of -150°C/h to room temperature. In order to avoid oxidation, the heat treatment was performed in a protective argon atmosphere.

The EBSD map in Fig. 1 shows the measured geometry and crystallographic orientations of the grains. The specimen was initially polished with abrasive SiC paper, diamond suspension and colloidal silica. DIC technique requires speckles on the surface under investigation. Before the speckle deposition, the surface of the specimen was etched using a solution of 9 ml H2O + 10 ml HCl + 1ml HNO3 for 6 minutes. Six markers, applied by Focused Ion Beam (FIB), define a square area on the central region of specimen's surface to be investigated. This information is used in both, the numerical model and the measuring and interpretation of the strain maps.

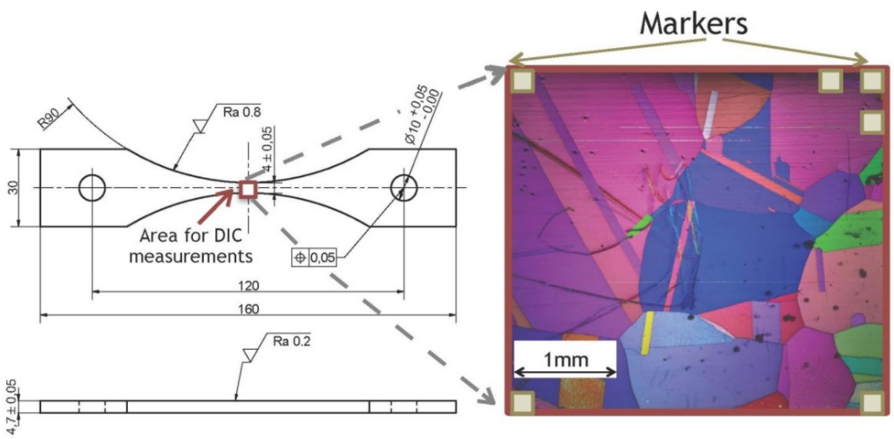

Figure 1: Specimen for tensile and fatigue testing with the marked area for DIC measurements

A tensile experiment was conducted with a MTS 370 (100 kN) servo-hydraulic loading frame. The set-up guaranteed uniaxial loading of the specimen, avoiding any bending or torsion. A load controlled tensile test were conducted and the average axial strains were measured in the center of the specimen to construct the stress-strain curve. In the experiments, local strains during and after the tensile test were measured, Herrera-Solaz, L. Patriarca, E. Foletti, J. Segurado, M. Niffenegger (2019). Real-time full field DIC local strain measurements during the specimen's deformation were performed by capturing the corresponding images with a 2 Megapixel Allied Vision Manta CCD camera, equipped with an optical lens system produced by Qioptiq with a resolution of 2 μm/px.

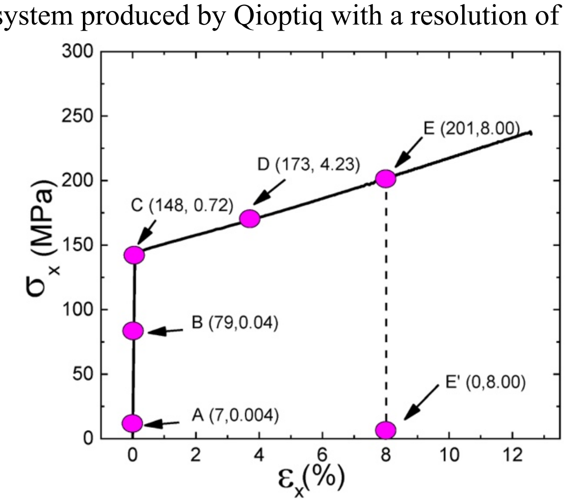

Fig. 2: Nominal (averaged) stress-strain curve

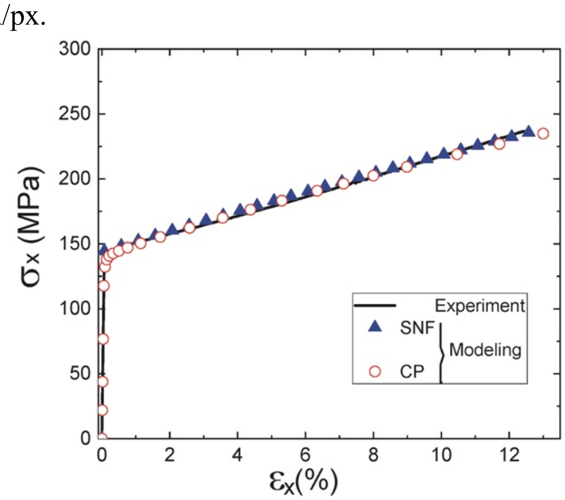

Fig. 3: Comparison of stress-strain curve, measured and calculated with the SNF and CAPSUL codes

The exposure time was set to approx. 0.2 sec/image to limit the noise. The images of the grain boundaries, acquired with the same microscope as used for DIC measurements, guaranteed a precise overlap between the microstructure and the strain measurements. The DIC reference image was initially captured at zero load, while the deformed images were captured with a rate of 5 img/sec. The x-axis is parallel to the loading direction, while the perpendicular direction corresponds to the y-axis. Figure 2 shows the points on the stress-strain curve, where the measured strains are compared with calculated ones. Figure 3 shows the experimental and calculated nominal stress-strain curve, which proves that the SNF modes captures the macroscopic stress-strain behavior rather well. This is a prerequisite for the correct calculation of the strains on the microscopy scale described in this paper. In-situ DIC measurements were performed at points B, C, D and E of Fig. 2, whereas ex-situ DIC measurements yield the residual strains at point E' (unloaded). However, in the following we compare measured and calculated local surface strain fields ε_x of the aforementioned sample at two load points C and E' of the tensile test.

COMPARISON OF MEASURED AND CALCULATED LOCAL STRAINS AND STRESSES

The determination and modelling of microstructure follows the procedure described above. A FE model with dimensions Lx, Ly and Lz of 3744 × 3456 × 240 µm containing 58 grains was employed to study the strain distribution in the RVE due to tension loading. The superficial layer of the middle section of the sample was reproduced by a mesh of 24640 brick elements with a side length of 24 µm (see Fig. 4). The thickness of the model is 240 µm, consisting of 10 24 µm thick FE-layers. The simulation of the tensile test was carried out imposing a displacement along X to the side surface of the volume (x = Lx) and restricting that degree of freedom at plane x=0. Additionally, the displacement along Y and Z was set to zero at point R (0, 0.5Ly, 0.5Lz), in order to suppress rigid body motion. The set of single crystal properties h_0, τ_0,c and τ_{sat} (both for the SNF and CPFEM models) were obtained by fitting the calculated stress-strain curve (Fig. 3) with an inverse analysis, Herrera-Solaz et al. (2014), to the experimental results. For this purpose, a representative volume element (RVE) of the microstructure of 1000 orientations was employed (Fig. 5). The parameters used to model the constitutive response of the material are given in Tab. 1, together with the C_{ij}, $\dot{\gamma}_0$, m, a and q.

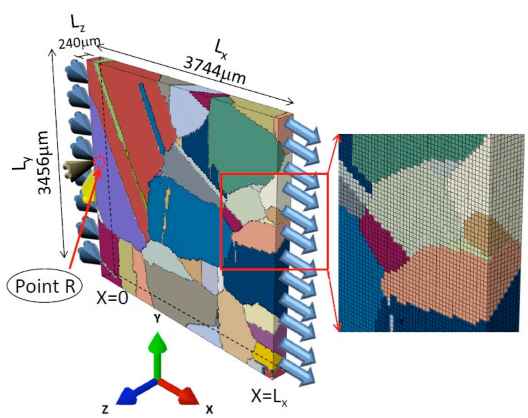

Fig. 4: The 3D-FE-model of the real micro-structure

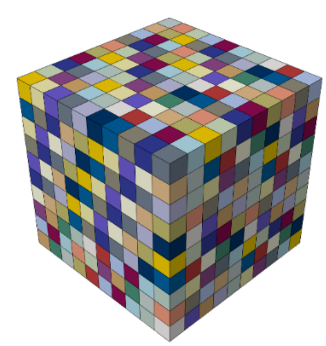

Fig. 5: The RVE used in the inverse analysis

The SNF and CPFEM models were employed to calculate the strain fields corresponding to the experimental findings. Figure 6 present the strains ε_x (in loading direction). Additionally, a frequency histogram of the strains (Fig. 7) with the overlaying Gaussian curves on the right quantitatively compares the different techniques. Regarding the longitudinal direction X, there is not only good agreement of the strain localization but also on the distribution of them. Note that both numerical models capture the strain concentrations from the first stage of deformation to the end of the test; this is clearly seen at points C and E' in Fig. 6. However, minor differences on the ε_x distribution can be seen at large strains (point E'), where the results of the SNF model show a pooling of data much closer to the mean value. In this sense, CPFEM appear to be more precise on mimicking the shape of the histogram at E' (Fig. 7). This was expected since CPFEM describes the material behavior by considering all the involved slip systems in the deformation process, unlike the SNF model, which only chooses the preferential one. This simplification is admissible for small and elastic strains within the grains/crystals of the material. CPFEM theory is more recommendable to capture large strains when multiple slip systems are activated. The threshold from where the SNF model loses accuracy seems to be much above the yield strength of the material (ε_x >3-4%). However, up to this point, the SNF model, which was developed to analyze small strains (LCF and HCF), shows quasi-identical results as CP. However, especially for complex FE models and many iteration steps, the computational time needed for the SNF model is significantly reduced.

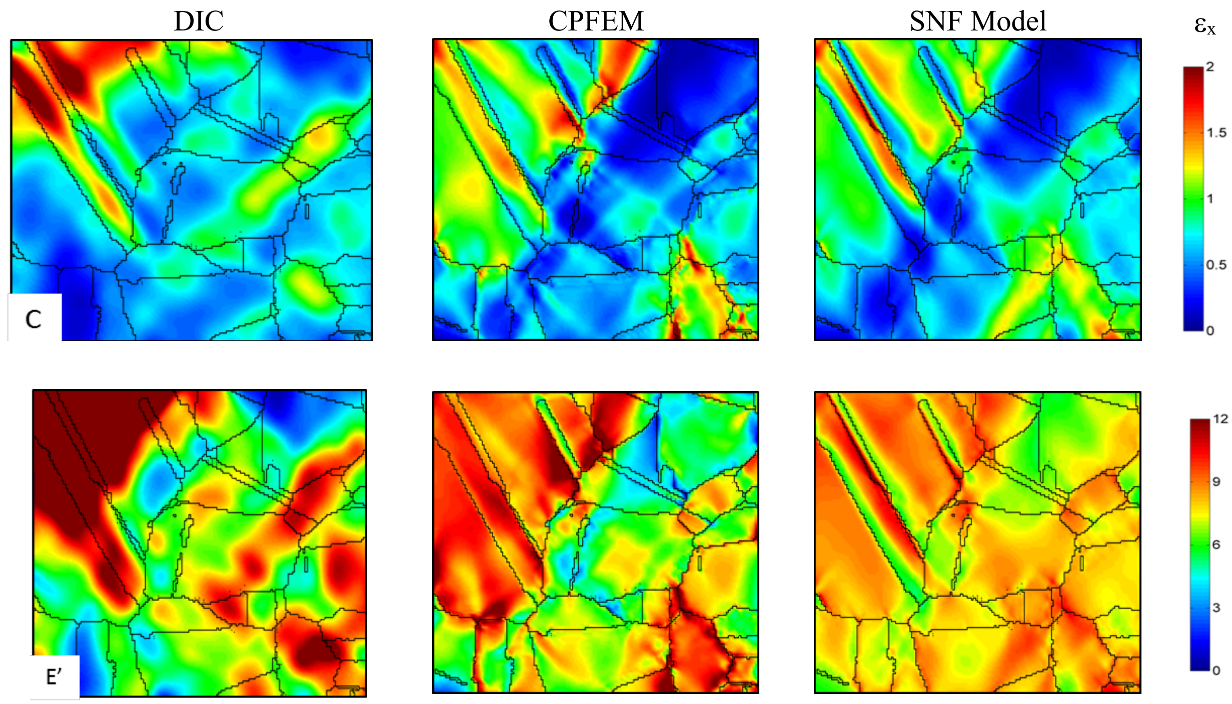

Figure 6. Calculated and measured strains in longitudinal direction X at points C and E'

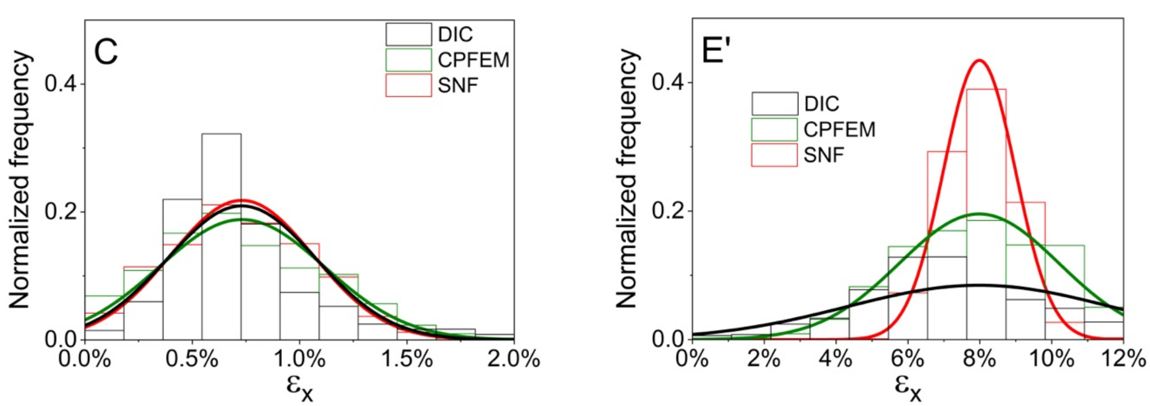

Figure 7. Histograms of ε_x frequencies at points C and E'

In contrast to measured strain fields, stress fields can only be calculated. However, the FE models showed an acceptable agreement of the strain maps with the experimental results; therefore, it is admissible to compute stress. In Fig. 8 the maps of longitudinal stresses σ_x at different load points, before (points B) and after yielding (E) in Fig. 3, are presented. If the macroscopic load is below the yield strength, small differences between the models can be neglected as shown in the maps and histograms of points B. Moreover, small stress concentrations start to appear at the grain boundaries. This phenomenon is most evident at points C (not shown) and particularly at E. CPFEM simulations capture these spots more accurately than the SNF model as well as a wider range of stress fields. This phenomenon, observed at the histogram, where the standard deviation of SNF distribution is getting smaller from point C on. The values of the maximum stresses are also of interest since it may explain local damage, especially for HCF, where macroscopic stresses are below the endurance limit. In general, there is almost a factor of two between the applied macroscopic stress and the maximum local stresses.

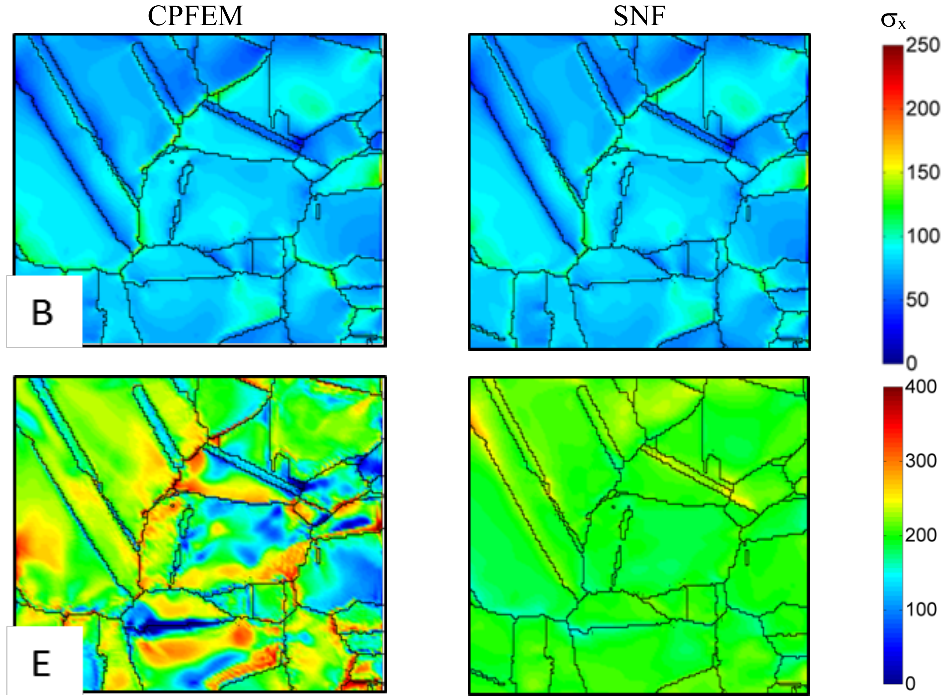

Figure 8. Calculated stresses in longitudinal direction X at points B and E

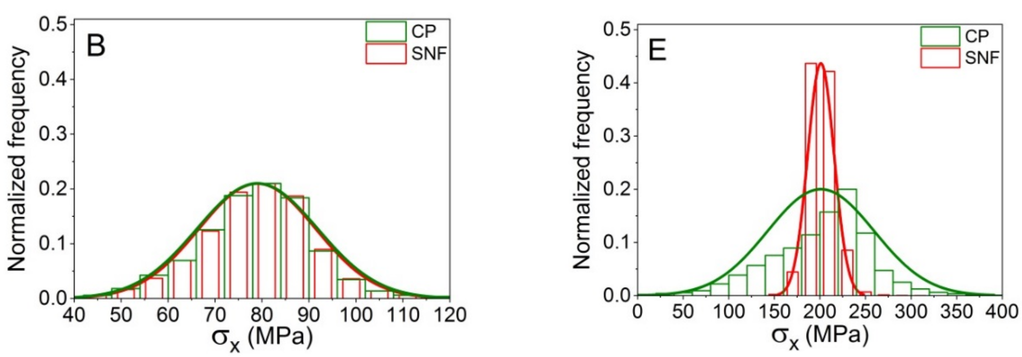

Figure 9. Histograms of σ_x frequencies at points B and E

For example, the macroscopic stresses at points B and E are 79 and 201 MPa, respectively (Fig. 3). However, the microscopic stresses rise approximately up to 120 and 400 MPa (Figs. 8 and 9); this may be a reason or could justify the appearance of micro-cracks at the grain level even under small strains, as it is the case for high cyclic fatigue loading.

CONCLUSIONS

In the present work, we present microstructure-based finite element simulations and DIC measurements to evaluate local strain fields on the microstructural scale of an austenitic stainless steel 316L during tension loading. Within the elastic range, strain maps (measured and predicted) in longitudinal and transverse direction of a representative volume element showed good agreement between the results of crystal plasticity code CAPSUL and SNF model and with experimental observations. However, at large plastic strains (ε>4%) only CPFEM approach was able to reproduce strains within the microstructure with high accuracy. This was expected since the simple model SNF model was developed mainly for fatigue analyses and not for large strains. The corresponding stress maps calculated by CPFEM and SNF showed excellent agreement for loads below the yield strength of the material. However, the stress maps from SNF at higher strains showed much less variability of the stresses between the different grains and their boundaries, in comparison with CPFEM results. An important result of the described analysis is that the local stress peaks appeared to reach twice the nominal (macroscopic) value. We also conclude that the DIC method is a valuable technique to measure the distribution of strains on the microscopic scale. Its results are comparable with those of the numerical models.

ACKNOWLEDGMENT

The authors would like to thank swissnuclear for funding this research within the project PLiM (swissnuclear frame contract No.1310), Dr. L. Patriarca and Prof. Dr. S. Foletti from Politecnico di Milano for performing the DIC measurements. We also thank Hans Kottmann for his support in performing the EBSD measurement and his excellent experimental support.

REFERENCES

Abaqus. (2014). *Analysis user's manual, version 6.14*, Dassault Systemes; 2014.

Cipiere, M.F., Le Duff, J.A., (2001). "Thermal fatigue experience in French piping, influence of surface condition and weld local geometry", *Document IIW-XII-1891,* Ljubljana, Slovenia.

Cipiere, M.F., Goltrant, O., (2002). "Circuit RRA N4, Incident de Civaux 1", *Fontevraud 5,* Volume 2, pages 875-882, 23-27.

Darveaux R. (2002). "Effect of simulation methodology on solder joint crack growth correlation". *J Electron Packag 2002*; 124:147–54.

Deardorff, A. et. al. (2004). "A Survey of Current US Nuclear Plant Fatigue Issues", *International Conference on Fatigue of Reactor Components*, Seville, Spain, 4-6.

Faidy, C., (2000). "Thermal fatigue in French RHR systems, International conference on fatigue of reactor components"*, Int. Conf. on Fatigue of Reactor Components*, July 31–August 2, Napa.

Farukh F, Zhao L., Jiang R., Reed P., Proprentner D., Shollock B. (2016). "Realistic microstructure-based modeling of cyclic deformation and crack growth using crystal plasticity", *Comp Mater Sci 2016*; 111:395–405.

Fissolo, A., Maillot, V., Degallaix, G., Degallaix, S., Haddar, N., Roux, J.L., Stephan, J.M., Amzallag, C., Bouchet, F. (2004). "Multiple cracking under thermal fatigue", *La Rev. Met.,* 101 (12), 1087–1099.

Haddar, N., Fissolo, A. (2004). "2d simulation of the initiation and propagation of crack array under thermal fatigue", *Nucl. Eng. Des. 235*, 864–945.

Hirschberg, P., (2000). "Operating experience regarding thermal fatigue of un-isolable piping connected to PWR reactor coolant systems", *International Conference on Fatigue of Reactor Components*, Napa. July 31-August 2.

Herrera-Solaz, V. and Niffenegger, M. (2017), "Application of hysteresis energy criterion in a microstructure-based model for fatigue crack initiation and evolution in austenitic stainless steel", *Int. J. of Fatigue 100* (2017) 84-93.

Herrera-Solaz V., Segurado J., LLorca J. “On the robustness of an inverse optimization approach based on the Levenberg–Marquardt method for the mechanical behavior of polycrystals”, *Eur J Mech-A/Solids 2015*; 53:220–8.

Herrera-Solaz V., LLorca J., Dogan E., Karaman I., Segurado J. (2014). “An inverse optimization strategy to determine single crystal mechanical behavior from polycrystal tests: Application to AZ31 Mg alloy*”, Int J Plast 2014*;57:1–15.

Herrera-Solaz V., Patriarca L., Foletti S., Segurado J. Niffenegger M. (2019). “Microstructure-based modelling and Digital Image Correlation measurement of strain fields in austenitic stainless Steel 316L during tensión loading”, Material Science & Engineering A 751, 99-106.

Herrera-Solaz V., LLorca J., Dogan E., Karaman I., Segurado J., “An inverse optimization strategy to determine single crystal mechanical behavior from polycrystal tests: Application to AZ31 Mg alloy”, International Journal of Plasticity 57 (2014) 1

Janssens, K.G.F., Niffenegger, M. and Reichlin, K. (2008). “A computational analysis of cyclic thermal shock induced elasto-plastic ratcheting”*, Nucl. Eng. Des. 239*, 36-44.

Korsunsky A. Dini D., Dunne F., Walsh M. (2007). “Comparative assessment of dissipated energy and other fatigue criteria”, *Int J Fatigue 2007*;29(9–11):1990–5.

Kothari M., Anand L., “Elasto-viscoplastic constitutive equations for polycrystalline metals: Application to tantalum”, Journal of the Mechanics and Physics of Solids 46 (1) (1998) 51 { 83.

Metzner, K.-J., Wilke, U. (2005). “European THERFAT project—thermal fatigue evaluation of piping system Tee-connections”, *Nucl. Eng. Des. 235*, 473–484.

Meneghetti G., Ricotta M., Lucchetta G., Carmignato S. (2014). “An hysteresis energy-based synthesis of fully reversed axial fatigue behaviour of different polypropylene composites”, *Compos Part B:Eng 2014;* 65:17–25.

NEA/CSNI/R(2005)8. “Thermal cycling in LWR components in OECD-NEA member countries”, *NEA/CSNI/R(2005)8*.

Niffenegger, M., Janssens, K.G.F. & Reichlin, K., (2009). “Experimental and Numerical Investigation of Cyclic Thermal Shock at the Paul Scherrer Institute”, 20th International Conference on Structural Mechanics in Reactor Technology (SMiRT-20), Espoo, Finland, August 9-14.

Niffenegger, Herrera-Solaz (2017), “Modeling of high cycle fatigue crack initiation and growth based on real polycrystalline microstructure”, 24th International Conference on Structural Mechanics in Reactor Technology (SMiRT-24), Busan, Korea, August 20-25, Doc No. 650, D1, Paper ID 01-06-06.

OECD Nuclear Energy Agency, (2006). “Nuclear power plant operating experiences from the IAEA/NEA incident reporting system 2002–2005”, *Tech. Rep. NEA No. 6150*.

Sistaninia M., Niffenegger M. (2014). “Prediction of damage-growth based fatigue life of polycrystalline materials using a microstructural modeling approach”, *Int J Fatigue 2014*; 66:118–26.

Sistaninia M., Niffenegger M. (2015). “Fatigue crack initiation and crystallographic growth in 316L stainless steel*”, Int J Fatigue 2015;* 70:163–70.

Segurado J., Llorca J. (2013), “Simulation of the deformation of polycrystalline nanostructured Ti by computational homogenization”, Computational Materials Science 76, 3.

Taylor G., (1938), “Plastic strain in metals”*, Inst. Met., 62 (1938), pp. 307-324.*